Author's Accepted Manuscript

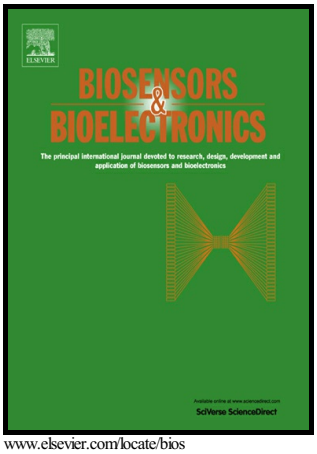

www.elsevier.com/locate/bios

The insight study of SnO pico size particles in an ethanol-water system followed by its biosensing application

Ammara Ejaz, Seungwon Jeon

PII: S0956-5663(18)30429-9
DOI: https://doi.org/10.1016/j.bios.2018.06.004
Reference: BIOS10524

To appear in: *Biosensors and Bioelectronic*

Received date: 8 May 2018
Revised date: 30 May 2018
Accepted date: 2 June 2018

Cite this article as: Ammara Ejaz and Seungwon Jeon, The insight study of SnO pico size particles in an ethanol-water system followed by its biosensing application, *Biosensors and Bioelectronic,* https://doi.org/10.1016/j.bios.2018.06.004

This is a PDF file of an unedited manuscript that has been accepted for publication. As a service to our customers we are providing this early version of the manuscript. The manuscript will undergo copyediting, typesetting, and review of the resulting galley proof before it is published in its final citable form. Please note that during the production process errors may be discovered which could affect the content, and all legal disclaimers that apply to the journal pertain.

ACCEPTED MANUSCRIPT

The insight study of SnO pico size particles in an ethanol-water system followed by its biosensing application

Ammara Ejaz[1], Seungwon Jeon[1*]

Department of Chemistry and Institute of Basic Science, Chonnam National University, Gwangju 500-757, Republic of Korea.

[*]Corresponding author. swjeon3380@naver.com

Accepted manuscript

Abstract

Pico sized Stannous oxide particles (SnO PPs) were synthesized in an ethanol-water solvent system on the surface of nitrogen doped graphene oxide (GO). The highly conductive support was a combination of dual interactions between 4-aminomethylbenzylamine (AMBA) and GO. The oppositely positioned $-NH_2$ linkers of the AMBA were covalently incorporated into the GO matrix through condensation reaction followed by the strong $\pi - \pi$ stacking interactions between aromatic rings of AMBA and GO. The change in the local chemical environment of GO via dual interactions provided a suitable atmosphere for the growth and dispersion of SnO PPs on GO-AMBA surface. The possible mechanism for the formation of SnO in an ethanol-water solvent system was evaluated. Furthermore, a light was shed on the factors responsible for the pico size of SnO particles synthesis along with its phenomenal distribution on the GO-AMBA surface.

[1] Tel.: +82 62 530 0064; fax: +82 62 530 3389.

ACCEPTED MANUSCRIPT

The catalyst containing SnO PPs was deployed as a biosensor for the detection of ascorbic acid (AA) for the very first time. A very wide linear range of 5.0×10^{-5}–7.0×10^{-3} M, limit of detection (LOD) of 1.19×10^{-5} M along with excellent practical feasibility, storage stability, repeatability and selectivity towards AA electrooxidation showed the excellent synergy between nitrogen-rich GO surface and SnO PPs. The sensitivity (885.54 $\mu AmM^{-1}cm^{-2}$) of the catalyst was the most attractive feature, as it was obtained in the presence of 5 and 2-fold higher concentration of UA and DA interfering species respectively.

Keywords: Graphene oxide; 4-aminomethylbenzylamine; Covalent and π – π stacking interactions; SnO PPs; Ethanol solvent; AA electrooxidation

Accepted manuscript

1. Introduction

AA, an indispensable microcurrent in the human body has not only influenced various physiological processes such as, enhancing antibody formation (Sinha et al., 2017), promoting iron uptake (Jin et al., 2009), activation of biological defense mechanism and cell division (Dong et al., 2013) but also holds a standard role in the cosmetics industry due to its anti-aging behavior (Sliem et al., 2017). Conversely, scurvy, and hypoimmunity roots from the deficiency of AA in the human body, while diarrhea, acquired immune deficiency syndrome, coronary heart disease and hyperacidity are the results of an excessive AA concentration (Agarwal et al., 2015). To deal with these glitches, the monitoring of accurate AA concentration is of paramount significance. Heretofore, a lot of efforts have been made to detect AA using chemiluminescence (Chen et al.,

ACCEPTED MANUSCRIPT

2017), capillary electrophoresis (Wang et al., 2018), colorimetry (Ji et al., 2018), polarography (Sahbaz and Somer, 1992), spectrophotometry (Shiri et al., 2017), liquid chromatography (Turak et al., 2017), titration with an oxidizing agent (Paim et al., 2002), electrochemistry (Pisoschi et al., 2014) etc. Though these techniques fulfill the demand of sensitivity, amidst all, electrochemistry gives the best response due to its ease of operation, low detection capability, excellent selectivity and portability.

Metal oxides (MOx) having nanostructure forms hold a pronounced reputation for a number of applications due to their significant surface to volume percentage. The high surface area to volume ratio of nanoparticles (NPs) provides a remarkable driving force for diffusion of analytes (Liufu et al., 2005). The synthesis of metal particles (either nano or pico) initially involves nucleation, which is followed by its growth (Thanh et al., 2014). A detailed atomic understanding of the mechanisms of nucleation and growth stages during metal particles formation is still not completely understood. However, theories like LaMer mechanism (Mer, 1952), Ostwald ripening (Ostwald, 1900), digestive ripening (Lee et al., 2005), Finke-Watzky two-step mechanism (Watzky and Finke, 1997), intraparticle ripening (Peng et al., 2000), coalescence and orientated attachment (Niederberger and Cölfen, 2006) provides an outline about what occurs within different systems. During NPs synthesis, surface energy, charge, solvation and surrounding chemical environment are relevant parameters to be considered. The interactions between the NPs – NPs and the NPs – fluid crucially determine the fate of individual and collective NPs. The NPs have high surface energy, are unstable, and tend to agglomerate or undergo coalescent either by van der Waals, electrostatic or magnetic forces. The counteractive repulsive forces from electrostatically stabilized NPs are described to have at least one electrical double layer due to a surface charging. The resulting Coulomb repulsion forces between the

Accepted manuscript

ACCEPTED MANUSCRIPT

particles decay exponentially with a particle to particle distance. If the electrostatic repulsion is sufficiently high, it prevents the particles from any kind of coagulation (Polte, 2015).

Among all MOx, stannous oxide (SnO) is an inexpensive environment-friendly p-type semiconductor with a band gap of 2.5–3 eV (Pires et al., 2008)). The surface of SnO has Sn^{2+} as Lewis acid and O_2^- as Lewis base center which accelerates the reaction rate. The fabrication of SnO has been a challenging task due to the possession of a dual valency characteristic of tin oxides (stannic (SnO_2) and SnO). Therefore, infrequent literature is available regarding its potential applications. Only a hand full of studies suggests SnO as a good catalyst for gas sensors (Hien et al., 2014), thin-film transistors (Luo et al., 2017) and an anode material for lithium-ion batteries (Song et al., 2016). To integrate the SnO PPs on a surface, graphene and graphene derived materials provide unique characteristics. We are all, very well familiar with the applications of graphene and GO in transistors (Kiani et al., 2017), lithium-ion batteries (Ajuria et al., 2017), solar cells (Xu et al., 2017), gas separation (Yoo et al., 2017), fluorescent biosensors (Zhang et al., 2017) and electrochemical sensors (Ejaz et al., 2017) due to their remarkably high surface-to-volume ratio, mechanical properties, thermal stability, fast electron transfer kinetics, flexibility, and electronic conductivity. Herein, we determined to improve the electronic conductivity of GO from the additional electron of a nitrogen atom. The literature reveals that electron-rich nitrogen species activates the π electrons of the GO matrix and creates the active sites (Ejaz and Jeon, 2017a). A derivative of benzylamine molecules, AMBA, having two amino linkers on opposite sides acts as a stabilizer for metal PPs. These oppositely positioned $–NH_2$ groups are suitable to react with an acid group via a condensation reaction to form a C–N bond. Besides, the π electronic system of AMBA is also expected to improve the electron transfer rate through π-π stacking interaction with GO, resulting in a large surface-

Accepted manuscript

ACCEPTED MANUSCRIPT

active-group-to-volume ratio. Furthermore, the contact of small-sized SnO PPs with chemically N-doped GO would enhance charge carrier mobility of the catalyst by increasing its surface area hence improving the accessibility of the analyte molecules to the catalyst surface.

Herein, we report the synthesis of SnO PPs along with its successful dispersion on the surface of nitrogen doped GO nanomaterial (GO-AMBA). The SnO PPs were synthesized in an ethanol-water solvent system rather than other solvents because of the exceptional dispersion and superior stability of metal oxides in ethanol (Safaei-Ghomi et al., 2014). The synthesis of GO-AMBA-SnO was done simply by chemical reduction and applied as a biosensor for the detection of AA. To the best of our knowledge, the electroanalytical application of SnO PPs as a biosensor for the detection of AA has not been unveiled. The electrochemical behavior of GO-AMBA-SnO was comprehensively studied via cyclic voltammetry (CV), differential pulse voltammetry (DPV), and chronoamperometry (CA) in 0.1 M phosphate-buffer saline (PBS, pH 7.4). In addition to the electrochemical study, the successful synthesis of SnO and incorporation of AMBA into GO was evaluated from the X-ray photoelectron spectroscopy (XPS), energy dispersive X-ray (EDX), Fourier-transform infrared spectroscopy (FTIR), Raman spectroscopy and X-ray diffraction (XRD). Whereas, the surface morphology, including the size, population of PPs, lattice line, and elemental mapping was extensively studied through high-resolution transmission electron microscopy (HRTEM).

Accepted manuscript

2. Experimental

2.1 *Chemicals and Reagents*

ACCEPTED MANUSCRIPT

Graphite powder (~325 mesh, 99.999%), AMBA, tin chloride ($SnCl_2$) hydrazine monohydrate ($N_2H_4.H_2O$), AA, dopamine (DA), uric acid (UA), and ethanol were purchased from Sigma-Aldrich Chemical Co., South Korea. $KMnO_4$, H_3PO_4, H_2SO_4, $NaH_2PO_4{\cdot}2H_2O$, and $Na_2HPO_4{\cdot}12H_2O$ were purchased from Daejung Co., South Korea. The 0.1M PBS was prepared from $NaH_2PO_4{\cdot}2H_2O$, and $Na_2HPO_4{\cdot}12H_2O$ and was employed as a supporting electrolyte for electrochemical studies. All the reagents used in this experiment were of analytical grade and were used without further purification. High purity argon (Ar) was used for deaeration. All electrochemical experiments were performed at room temperature.

2.2 *Instrumentation*

Electrochemical measurements were performed on an electrochemical workstation (CH Instruments Inc., USA) using a conventional three-electrode cell. The three-electrode cell configuration consisted of Pt as the counter electrode, Ag/AgCl (3.0 M NaCl solution) as the reference electrode and glassy carbon electrode (GCE, 3 mm diameter) as the working electrode. CV's were recorded between -0.8 and 0.8 V (vs. Ag/AgCl) in 0.1 M PBS, pH 7.4 with a scan rate of 0.05 Vs^{-1}. The DPV analysis was monitored at an amplitude of 0.05 V, a pulse width of 0.2 s and pulse period of 0.5 s. The CA study was evaluated at an applied potential of 0.1V. The pH measurements were performed using a JENCO pH meter with a glass electrode.

The structural characterization of the material was carried out using XPS on a MultiLab 2000 spectrometer (Thermo VG Scientific, Southend-On-Sea, Essex, UK) in an ultra-high vacuum chamber. The HRTEM and EDX was studied using a JEM-2100F microscope at 200 kV. The XRD spectrum was carried out on a Rigaku D/max-2500, using filtered Cu Kα radiation. The FTIR analysis was performed on Perkin Elmer Spectrum Two FTIR Spectrometer. Raman

Accepted manuscript

ACCEPTED MANUSCRIPT

spectra were obtained with LabRam HR800 UV Raman microscope (Horiba Jobin-Yvon, France), with an excitation of 515 nm Ar^{+} laser.

2.3 *Synthesis of GO-AMBA-SnO*

GO was synthesized from natural graphite powder (~325 mesh, 99.999%) according to the improved Hummer's method (Ejaz et al., 2016). The synthesis of GO-AMBA-SnO nanomaterial is shown in figure 1. Initially, GO was dispersed in double distilled water (1 $mgmL^{-1}$) and sonicated for 1 h. The resulting homogeneous suspension was mixed with an aqueous solution of AMBA (1 $mgmL^{-1}$) in a round-bottom flask equipped with a magnetic stirrer bar. After 2h of continuous stirring, a solution of $SnCl_2$ in ethanol (2 $mgmL^{-1}$) was added to the homogeneous solution and kept for 30-minute stirring. Thereafter, 100 µL of $N_2H_4.H_2O$ was added as a reducing agent followed by stirring along with heating at 110 ºC for the next 10 h. The black solution obtained was filtered three times with double distilled water and was dried under vacuum at 50 °C for overnight. For comparison, GO-AMBA and GO-SnO were also prepared in the same protocol except with the addition of $SnCl_2$ and AMBA respectively.

Accepted manuscript

ACCEPTED MANUSCRIPT

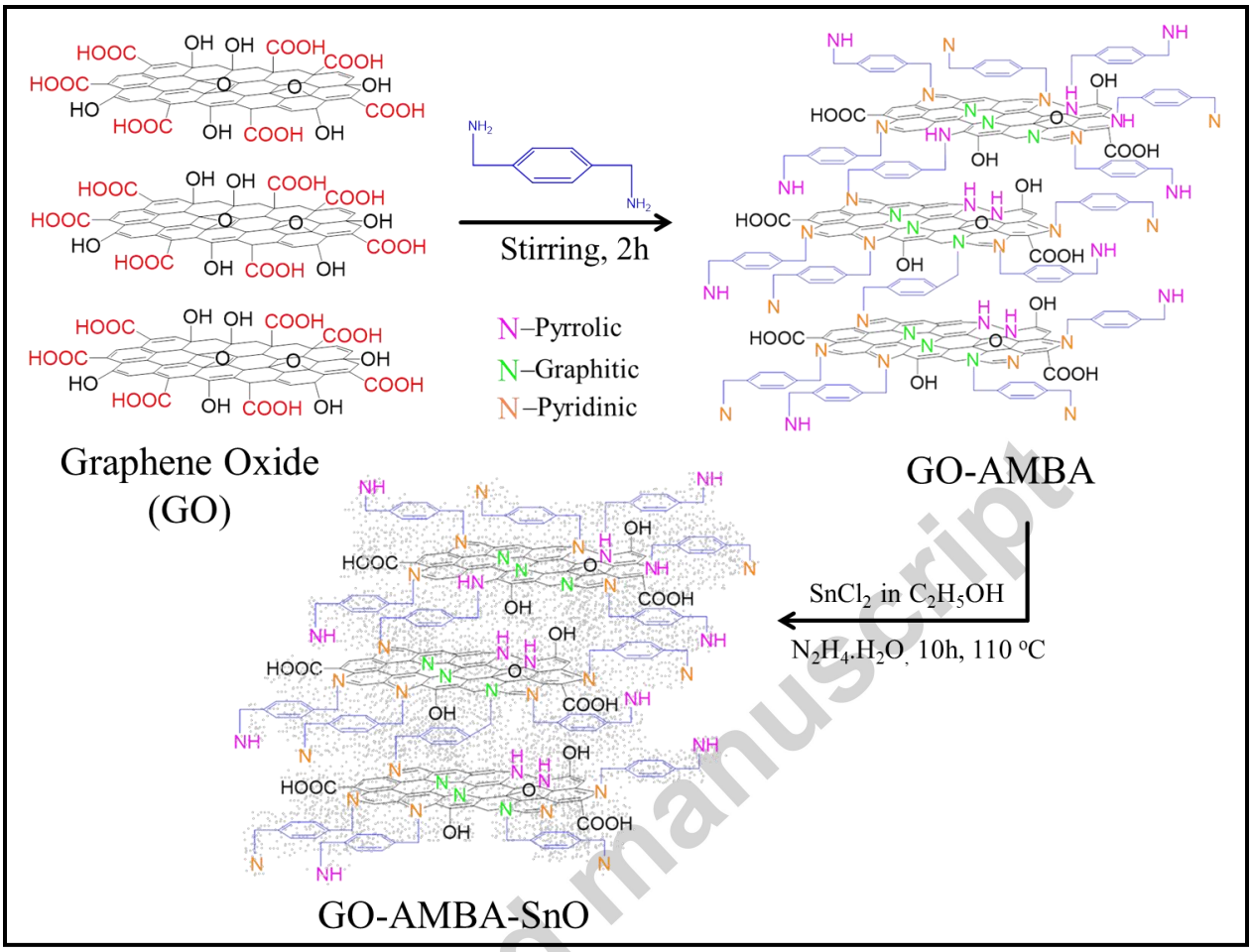

2.4 *Preparation of GO-AMBA-SnO modified electrode*

For the electrochemical study, GCE was polished with 0.05 µM alumina slurry. The adsorbed alumina from GCE surface was removed by thoroughly washing with methanol and double distilled water. After being carefully washed, 10 µL of the GO-AMBA-SnO solution (1 mgmL^{-1} H_2O) was coated on the surface of bare GCE. The GO-AMBA-SnO modified electrode was dried in air at room temperature. Finally, GO-AMBA-SnO modified electrode was immersed in 15 mL electrolytic cell containing deaerated 3 mL PBS.

3. Results and Discussion

Accepted manuscript

ACCEPTED MANUSCRIPT

3.1 Characterization of the catalysts

3.1.1 *Insight study of SnO PPs size and monodispersity*

Figure 2a shows the HRTEM image of GO-AMBA catalyst. As expected for nitrogen incorporation into the GO network, a wavy sheet having wrinkle and multi-layered structure was observed. These crumpled structures were most likely caused by the attachment of the N atom to the GO plane as a result of covalent functionalization (Larsen et al., 2016). On the other hand, a dense population of the exceptionally small sized SnO PPs was evenly dispersed on the GO-AMBA surface as shown in figure 2 (b, c, and d). TEM image taken at high resolution showed SnO PPs size in the range of 0.1–0.8 nm with a majority of the population between 0.2–0.5 nm range (inset; figure 2c). Further insights of SnO PPs was taken from the degree of crystallinity through lattice line. The PPs showed interlayer spacing of 0.267 nm corresponds to the (1 1 0) plane of SnO (Sakaushi et al., 2010) (inset figure 2e). The successful synthesis of GO-AMBA-SnO catalyst was evidenced from the elemental EDX spectra which showed distinct peaks of C, N, O with numerous Sn peaks along with EDX mapping as shown in figure 2 (e and f) respectively. The HRTEM analysis of GO-SnO nanomaterial discussed in the supporting information (figure S1) suggests that the incorporation of AMBA into GO tailored its electronic properties in such a way that the fabrication of SnO PPs was favored which ultimately resulted in the exceptional population of SnO PPs on the surface of GO-AMBA. Besides, the increased surface area through dual interactions also played a significant role by providing capacious space for the dispersion of SnO PPs.

Herein, the particle growth mechanism (figure 2g) initially includes the supersaturation of monomer SnO nuclei which lead to the formation of many small PPs. The second step involves

Accepted manuscript

ACCEPTED MANUSCRIPT

the formation of dimers and small clusters from metal oxide. Whereas, the third step covers the growth of particle due to aggregation and coalescence until reaching a final particle size at which the particles become sufficiently stable. At any time during the synthesis, the growth of particles is primarily correlated with colloidal stabilization, which determines the minimum particle size (Polte, 2015). The description of particle growth with colloidal stability is best explained by the DLVO theory derived in the 1940s. According to DLVO assumption, the interaction energy between two electrically charged approaching particles in suspension is the sum of Van der Waals attraction (VA) and electrostatic repulsion (VR) arising from the neighbouring double layers. When the two particles start to approach each other, the VR is stronger than the VA leading to an increase in the overall potential (V) with the decrease in the distance until a maximum is reached at VMAX, which corresponds to the repulsive energy barrier. As the distance is further decreased, the VA surpasses the VR (VA>VR), and the overall potential becomes strongly dominated by VA, which leads to the agglomeration of the particles. If VMAX>~10 kT (k is the Boltzmann constant and T the temperature), collision from Brownian motion will not overcome VMAX and agglomeration will not take place (Derjaguin and Landau, 1993; "VerweyOverbeek.pdf," n.d.). XPS spectra (figure 3c) have shown the dominance of pyrrolic and graphitic–N in GO-AMBA-SnO nanomaterial. Pyrrolic–N has an acidic H due to the delocalization of its lone pair. Thus, the repulsion between the acidic hydrogen of pyrrole and

Accepted manuscript

ACCEPTED MANUSCRIPT

positively charged graphitic–N is key to the monodispersion of SnO PPs.

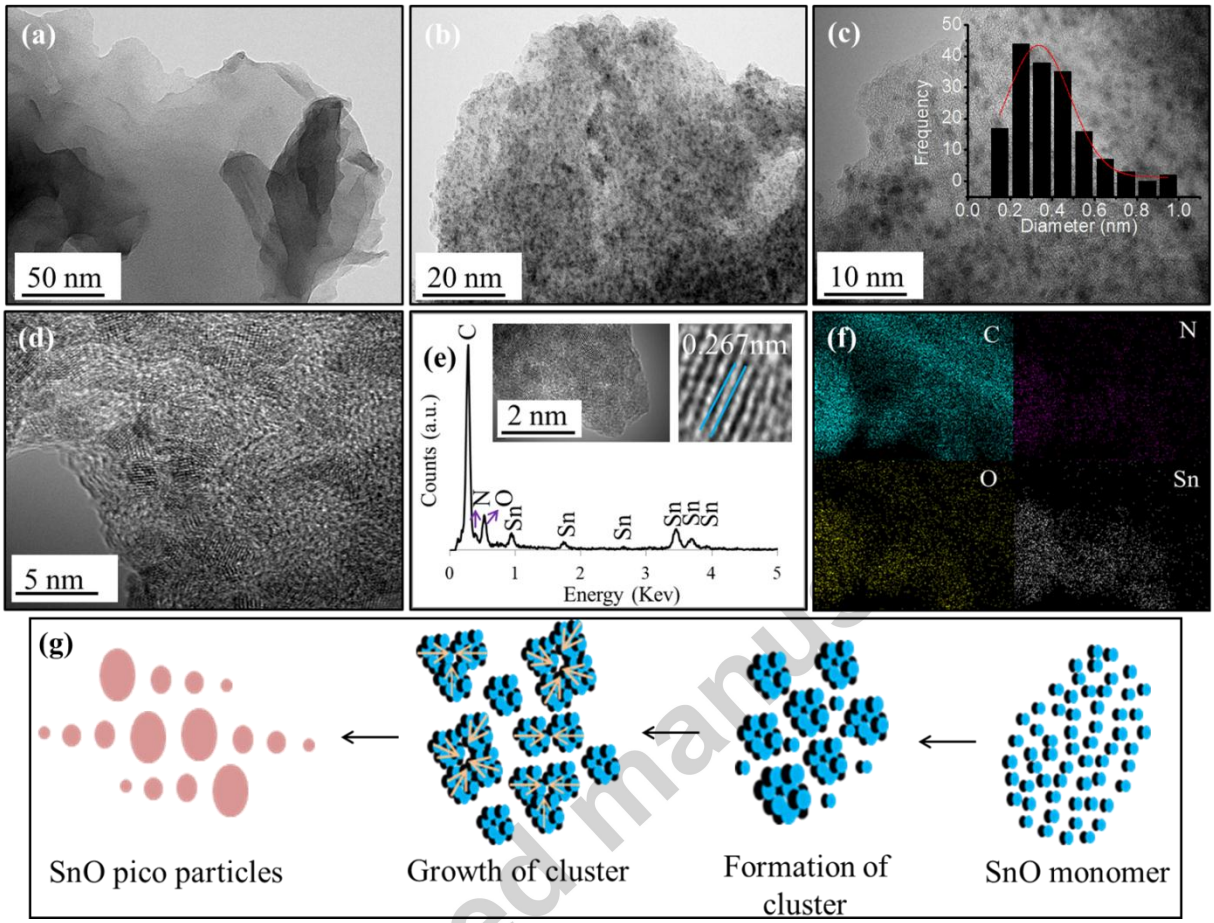

3.1.2 XPS study of GO-AMBA-SnO catalyst

XPS analysis was conducted to elucidate the formation of SnO PPs along with the successful incorporation of nitrogen into GO network. The survey spectra (figure 3a) of GO-AMBA-SnO nanomaterial showed a strong peak from carbon (C1s), nitrogen (N1s), oxygen (O1s) and two additional sharp peaks from Sn3d5 and Sn3d3 at 284.3 eV, 399.3 eV, 531.1 eV, 486.3 eV and 494.8 eV (Ejaz and Jeon, 2017b; Lu et al., 2013) respectively. The high-resolution spectra of C1s (figure 3b) emerged with three intense and a weak peak at 283.7 eV, 284.8 eV, 285.4 eV, 288.1 eV depicting the presence of C=C/C=N, C–C, C–O, and O–C=O respectively (Ejaz et al., 2018). A comparatively low intensity of O–C=O suggest the successful condensation reaction between

ACCEPTED MANUSCRIPT

–COOH group of GO and $–NH_2$ group of AMBA. Furthermore, the covalent functionalization of nitrogen species into the GO network was evidenced from the peaks of high-resolution N1s spectra (figure 3c) at 397.7 eV (pyridinic–N), 399.7 eV (pyrrolic–N) and 401.7 eV (graphitic–N) (Ejaz and Jeon, 2018a). The pyridinic–N bonds with two C atoms (sp^2 hybridized) at the edges or defects of graphene and contributes one p electron to the p system. The pyrrolic nitrogen occurs in a five-membered ring (sp^3 hybridized) and contributes to the p conjugated system with 2 p-electrons. Whereas, graphitic–N (sp^2 hybridized) which is also known as quaternary nitrogen refers to N atoms that substitute for C atoms in the hexagonal ring (Hien et al., 2014). It has been reported that the graphitic–N can help to improve the electrical conductivity of graphene, whereas pyridinic–N and pyrrolic–N can improve the electrochemical properties of GO in the electrochemical process (Cobo et al., 2012). The deconvoluted O1s spectra (figure 3d) of GO-AMBA-SnO provided confirmation of condensation reaction between –COOH group of GO and $–NH_2$ group of AMBA by showing a strong peak of the adsorbed water molecule at 533.3 eV. Literature suggests that tin exhibits three oxidation states Sn^0, Sn^{2+}, Sn^{4+}, with consecutive doublets of $Sn3d_{5/2}/Sn3d_{3/2}$ at 485.2 eV/493.9 eV, 486.4 eV/494.8 eV and 487.2 eV/495.4 eV respectively. The high-resolution Sn spectra in figure 3e showed $Sn3d_{5/2}$ peak at 486.2 eV and $Sn3d_{3/2}$ peak at 494.8 eV respectively, which corresponds to Sn^{2+} oxidation state. The spin energy gap of 8.6 eV between $Sn3d_{5/2}$ and $Sn3d_{3/2}$ confirmed the Sn^{2+} oxidation state (Song et al., 2011; Wang et al., 2009; Yang et al., 2012). Furthermore, the peak at 530.8 eV in figure 3d of O1s spectra also supported the formation of stannous oxide at GO-AMBA surface (You et al., 2013). Following is the possible mechanism of SnO formation in an ethanol-water system.

Accepted manuscript

ACCEPTED MANUSCRIPT

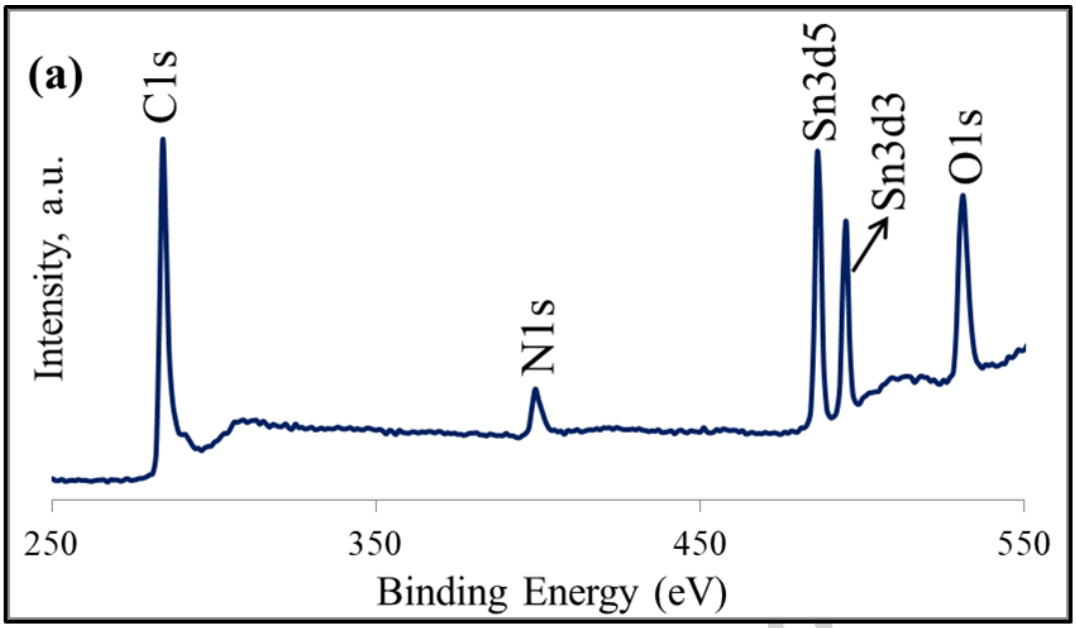

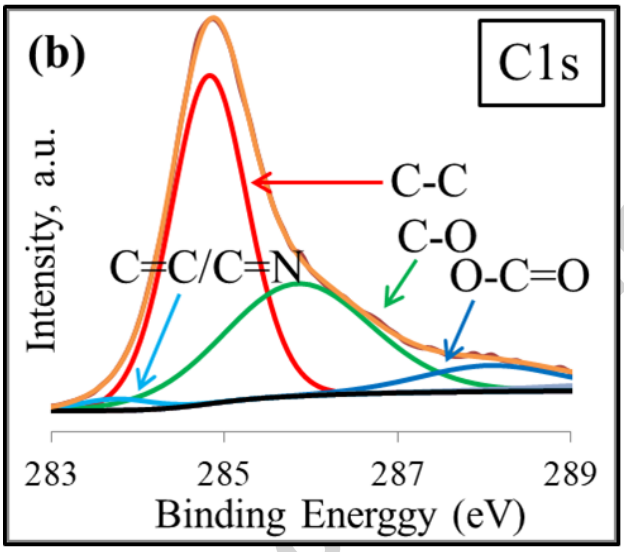

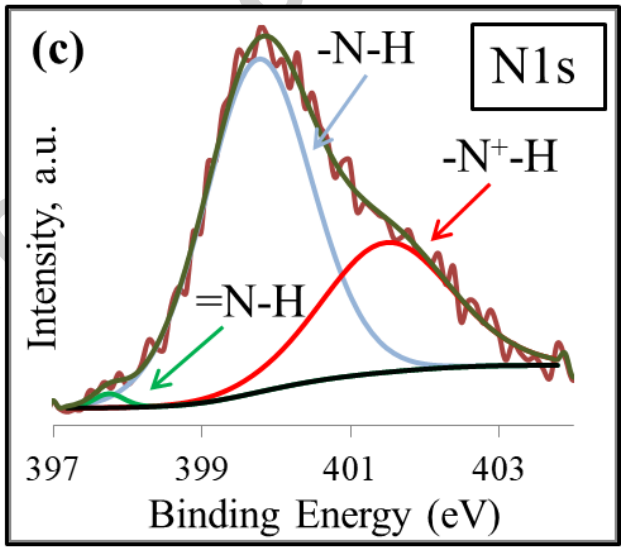

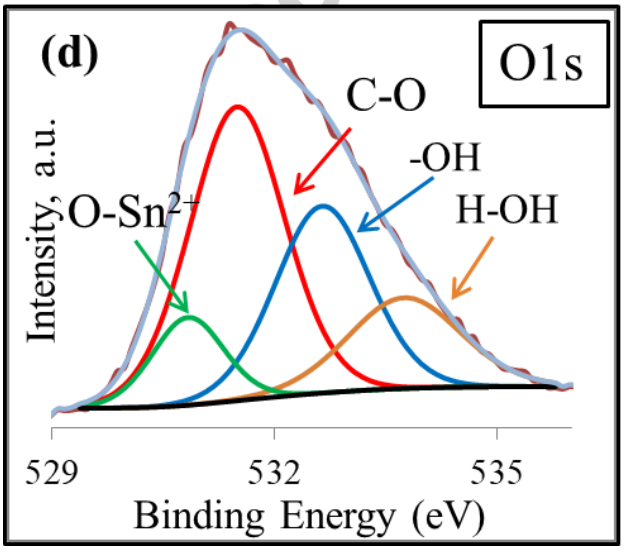

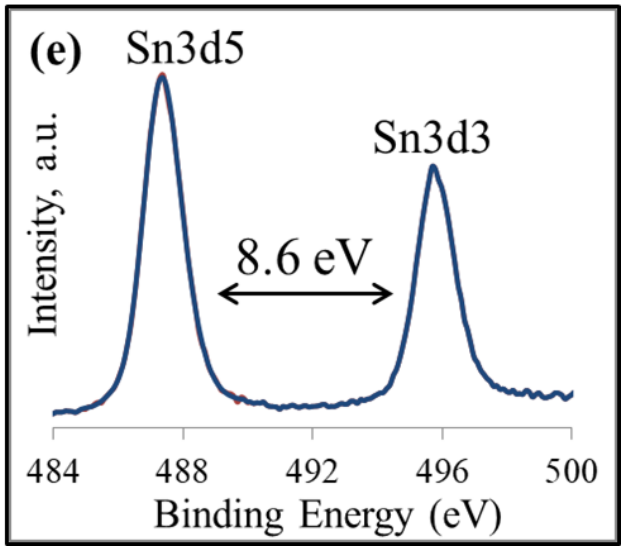

ACCEPTED MANUSCRIPT

3.1.3 Mechanism of SnO synthesis in an ethanol-water system

$SnCl_2$ easily oxidizes at temperatures around 100 ^oC into either +2 or +4 oxidation state. The acidic solution usually gives the dipositive ion (Sn^{2+}) whereas, in an alkaline condition dipositive tin (Sn^{2+}) disproportionate readily to tetrapositive tin (Sn^{4+}) and the free element ("Therald Moeller," n.d.). During synthesis of GO-AMBA-SnO, $SnCl_2$ was dissolved in absolute ethanol, a white fume appeared which was assumed to be hydrogen chloride gas (Uhlmann et al., 1984). The $SnCl_2$ reacted with absolute ethanol, according to the following equations.

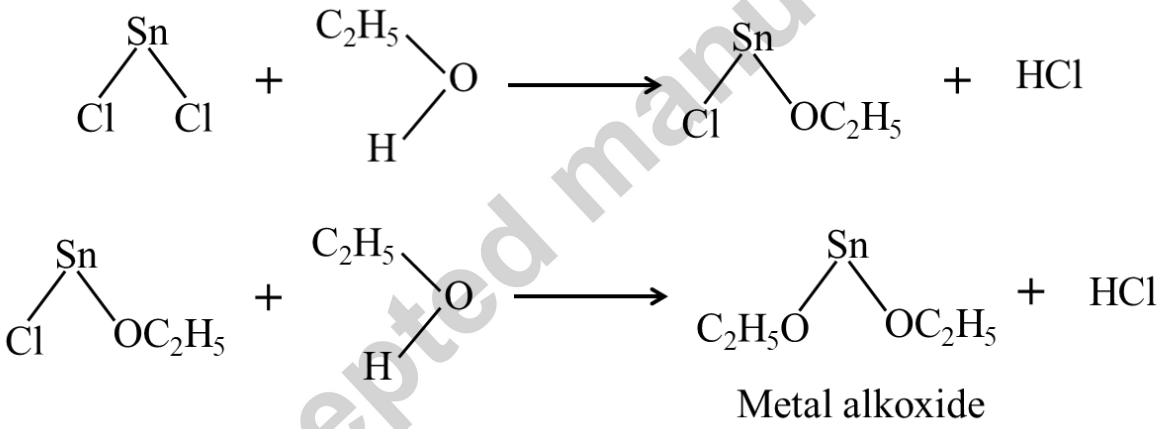

Metal alkoxides are in general very reactive due to the presence of highly electronegative OR groups (hard π donor) that stabilize metal in its highest oxidation state and render metal very susceptible to nucleophilic attack. The lower electronegativity of transition metals causes them to be more electrophilic and thus less stable towards hydrolysis, condensation and nucleophilic reaction. The thermodynamics of hydrolysis, alcoxolation and oxolation are governed by the strength of the entering nucleophile, the electrophilicity of metal and the partial charge and stability of the leaving group (Matsuo., 1988; Geffcken et al., 1939).

Accepted manuscript

ACCEPTED MANUSCRIPT

Transition metals often exhibit several stable coordination via oxolation, alkoxy bridging or other nucleophilic association mechanisms. For coordinatively saturated metals in the absence of a catalyst, hydrolysis and condensation both occur by nucleophilic addition followed by proton transfer from the attacking molecule to an alkoxide or hydroxo ligand within the transition state and the removal of protonated species either as alcohol (alcoxolation) or water (oxolation) resulting in the formation of M-O-M bond (Takeuchi, 1988).

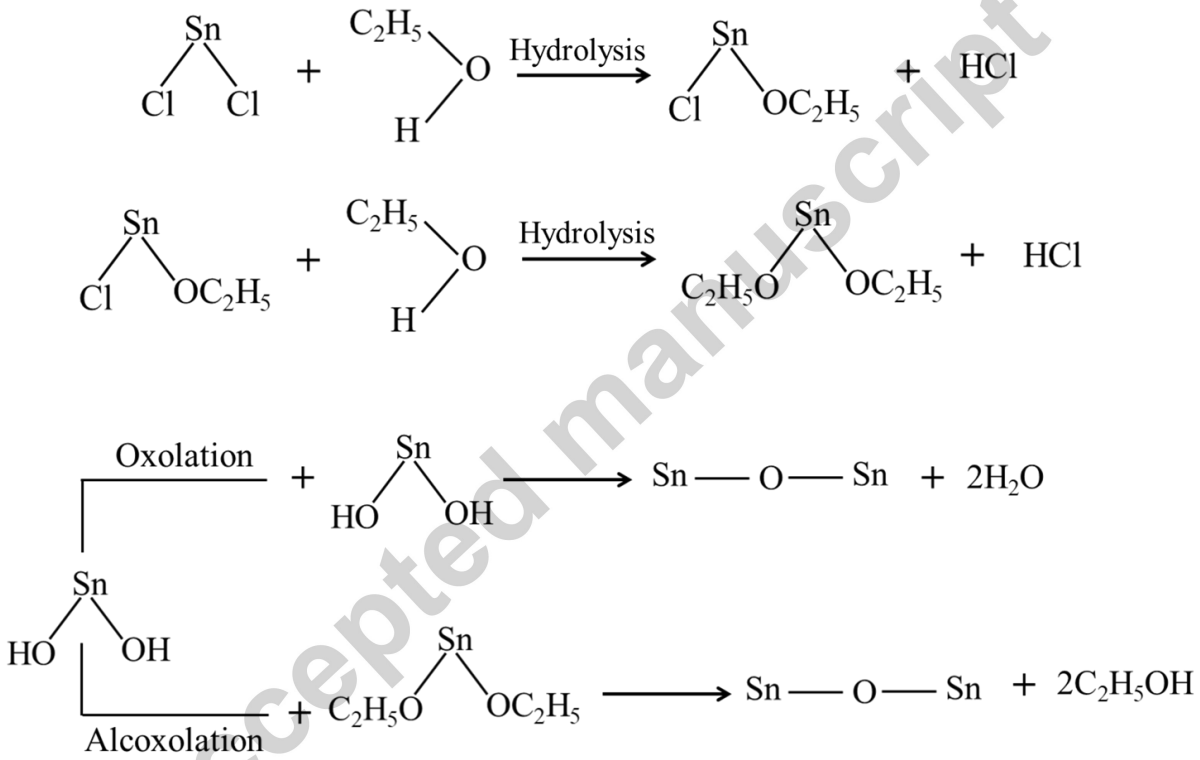

Accepted manuscript

3.1.4 Verification of GO-AMBA-SnO synthesis through FTIR, XRD and Raman spectroscopy

FTIR analysis of GO-AMBA-SnO (figure 4a) was performed in the frequency range of 450–3900 cm^{-1} to confirm the findings of XPS analysis. The CH in-plane bending vibrations usually occur in the region of 1430–990 cm^{-1} (Nagabalasubramanian et al., 2011). The peaks at 3378,

ACCEPTED MANUSCRIPT

1054, 2848, 2924 cm^{-1} are attributed to O–H, epoxy (Zhan et al., 2011), asymmetric and symmetric –CH stretching (Senthilnathan et al., 2014) respectively. Whereas, the peaks at 1202, 1534 corresponds to the C–N along with the peaks at 2076 (–CH=N), 2336 cm^{-1} (–CH–NH), which are possible in a ring-like structure (Senthilnathan et al., 2014). Moreover, the signal of the aromatic C=C stretching between 1610 to 1650 cm^{-1} indicates the presence of an sp^2 hybridized honeycomb lattice (Chen et al., 2015). Inset of the figure 4a shows a narrow range of FTIR spectrum in the frequency range of 500–1000 cm^{-1}. The peaks at <1000 cm^{-1} are all attributed to the Sn–O–Sn stretching (Seo et al., 2013).

Literature suggests that the XRD pattern of graphite has a definite peak at 26.54° corresponding to (0 0 2) plane having interlayer spacing (d) value of 0.33 nm. However, in case of GO, the peak is shifted to 11.07° having 'd' 0.79 nm. This shift is attributed to the exfoliation and complete oxidation of graphite (Geng et al., 2011). XRD pattern obtained from our synthesized nanomaterial GO-SnO, GO-AMBA and GO-AMBA-SnO are shown in the figure 4b. GO-AMBA nanomaterial showed a signature peak of nitrogen doping at 24.61° corresponding to the coherent and parallel stacking of graphene like-sheets signifying an increase in surface area. Another reflection obtained at 42.79° corresponds to the (1 0 0) plane, which suggests the honeycomb structure formation by sp^2 hybridized carbons (Wang and Shaikh, 2015). The (0 0 2) reflection in GO-AMBA-SnO and GO-SnO was shifted to 26.5° and 25.9° probably due to the further reduction of GO-AMBA and GO surface. Furthermore, clear, well-distinguished peaks of SnO at 33.48°, 51.2°, and 64.3° corresponding to (1 1 0), (1 1 2) and (2 0 2) face respectively were obtained from GO-SnO and GO-AMBA-SnO nanomaterial (Chen et al., 2014; Liu et al., 2014). The comparatively higher intensity of (1 1 0) and (1 1 2) SnO face suggests their preferred orientation at GO-AMBA and GO surface.

Accepted manuscript

ACCEPTED MANUSCRIPT

Raman spectra of all the catalysts were analyzed in the wavenumber range of 1000–2000 cm^{-1} (figure 4c). Generally, Raman spectra show two bands; the D band (at approximately 1350 cm^{-1}), which corresponds to a defect activated band originating in structural defects, edge effects and dangling sp^2 carbon bonds that break the symmetry, and the G band (at approximately 1590 cm^{-1}), which is assigned to the in-plane stretching motion between sp^2–C atoms. All nanomaterials (GO-SnO, GO-AMBA, and GO-AMBA-SnO) showed a prominent D band at 1350 cm^{-1} indicating the graphitic plane disorder originating from the sp^3–C atoms and/or heteroatoms associated in the sp^2–C network in a plane (Chen et al., 2014). On the other hand, the G band exhibited a very intense peak at ~ 1602 cm^{-1}. Based on the ratio of D and G bands, an estimate of defect densities was estimated among all catalysts. It was found that the synergistic effect of the dually interacted GO-AMBA having pico sized dispersed SnO particles showed higher degrees of defects (I_D/I_G = 1.11) as compared to the individual components (GO-AMBA, I_D/I_G = 0.89) and (GO-SnO, I_D/I_G = 0.94) of the catalyst.

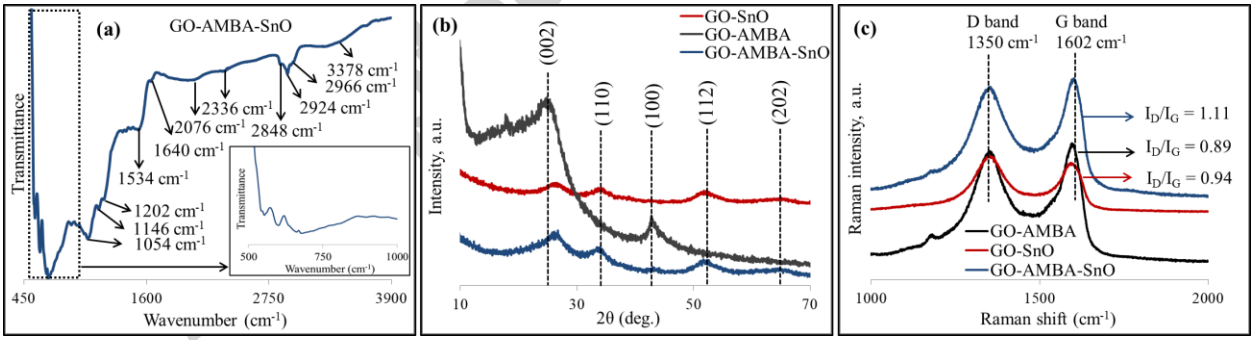

3.2 Electrochemical studies of GO-AMBA-SnO catalyst

3.2.1 Study of individual components of GO-AMBA-SnO catalyst towards AA electrooxidation

ACCEPTED MANUSCRIPT

The electrochemical study was started from evaluating the individual effect of each component of the GO-AMBA-SnO catalyst towards the electrooxidation of AA by performing CV's in 0.1M PBS (pH, 7.4) solution containing 5.0×10^{-3} M AA at 0.05 Vs^{-1}. The figure 5 comprises of four curves. Curve a shows, only the background current of GO-AMBA-SnO catalyst suggesting that no electrochemical reaction was conducted on the surface of GO-AMBA-SnO in the absence of AA. Whereas, the curve b, c and d show the response recorded in the presence of AA. Curve b (GO-AMBA), and c (GO-SnO) showed an obvious irreversible electrooxidation peak towards AA oxidation at a potential of 0.078, and -0.006 V with a current density of 3.07 $mAcm^{-2}$ and 3.12 $mAcm^{-2}$, respectively. As both modified electrodes showed AA electrooxidation at different potentials with a different intensity. So the individual effect of both catalysts was merged to gain the synergistic effect of nitrogen doping on GO and electron carrier mobility of SnO PPs. The synergy as expected was efficaciously found from the negative shift of oxidation potential along with an increment of 29 % in the current density (4.35 $mAcm^{-2}$) of the GO-AMBA-SnO catalyst.

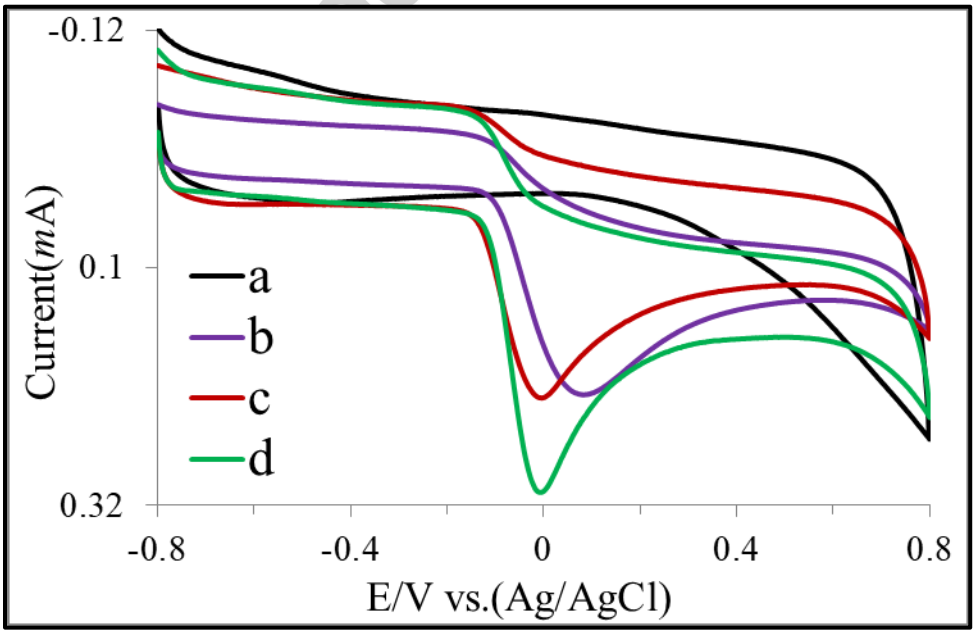

3.2.2 Kinetics followed by GO-AMBA-SnO catalyst towards AA electrooxidation

ACCEPTED MANUSCRIPT

In order to understand the AA electrooxidation process on GO-AMBA-SnO catalyst, CV was performed in PBS (pH, 7.4) solution containing 5.0×10^{-3} M AA at different scan rates (figure S2a). The electrooxidation current of AA continued to increase with the increase in scan rate along with the shift in oxidation potential from (-0.072 V $\rightarrow$ +0.201 V). When plotted (figure S2b), the electrooxidation current showed a linear relationship versus the square root of scan rate, depicting diffusion controlled kinetics of the GO-AMBA-SnO catalyst. The as-obtained statistics were further confirmed by plotting a graph between the logarithm of anodic peak current and logarithm of scan rate (figure S2c). As expected the graph came up with the slope value of 0.50 for a perfect diffusion controlled process suggested by the kinetic theory of the electrode reaction (Ejaz and Jeon, 2017a). The corresponding linear regression equations are given by;

$$I_{pa}\,(mA)_{AA} = 0.0463\,[\nu](mVs^{-1})^{1/2} - 0.0419,\ R^2 = 0.997$$

$$\log I_{pa}\,(mA)_{AA} = 0.509\,[\log \nu](mVs^{-1})^{1/2} + 1.6132,\ R^2 = 0.996$$

3.2.3 Evaluation of GO-AMBA-SnO catalyst through CA

Next on, the electrocatalytic activity of GO-AMBA-SnO catalyst towards AA electrooxidation was checked with respect to time using CA analysis. The Chronoamperograms were recorded at an applied potential of 0.1 V in PBS (pH, 7.4) solution as shown in the figure S3a. A steady current response was obtained even for the addition of a very small AA concentration (figure S3b) in the deoxygenated PBS, showing that the complementary interaction between nitrogen doped GO and SnO PPs has increased the accessibility of the AA molecule to its surface. The graph obtained from the electrooxidation current versus AA concentration (figure S3c) showed a

Accepted manuscript

ACCEPTED MANUSCRIPT

wide linear range of 5.0×10^{-5}–7.0×10^{-3} M with LOD and of 1.19×10^{-5} M. The corresponding linear regression equation is given by;

$$Ipa\ (mA) = 0.023 \times [C_{AA}]\ (mM) + 0.001,\ R^2 = 0.999$$

3.2.4 Selectivity of the GO-AMBA-SnO catalyst

One of the significant necessities of a biosensor is its anti-interfering ability. To evaluate the anti-interfering response, the DPV of GO-AMBA-SnO catalyst towards electrooxidation of AA was performed in the presence of DA and UA in PBS at optimized conditions. As shown in figure 6a, the addition of 5-fold higher concentration of UA showed an oxidation peak at 0.292 V. After single concentration addition of UA, AA was added to the PBS containing 5.0×10^{-3} M UA, GO-AMBA-SnO catalyst showed the same response as was obtained without the addition of UA (figure S4) in the PBS towards AA electrooxidation. The current response was monitored for various AA addition and when plotted against concentration (figure 6b), a linear range of 1.0×10^{-4}–1.0×10^{-3} M was obtained having correlation coefficient and a sensitivity of 0.996 and 796.89 $\mu A m M^{-1} cm^{-2}$ respectively. Similarly, in a fresh electrolyte (PBS), 1.0×10^{-3} M DA was added, a pronounced effect at 0.172 V was obtained showing the oxidation of DA by GO-AMBA-SnO catalyst. Thereafter, the addition of DA was stopped, and the addition of AA was begun from a predetermined amount. There was no effect on the efficiency of GO-AMBA-SnO catalyst towards electrooxidation of AA, in the presence of DA (figure 6c). This could be seen from the statistical data shown in figure 6d. A linear range of 1.0×10^{-4}–1.0×10^{-3} M was also found with a correlation coefficient of 0.999 and a sensitivity of 810.57 $\mu A m M^{-1} cm^{-2}$. After studying individual interference response, the next target was to monitor the response of GO-AMBA-SnO towards different concentrations of AA in the presence of both analytes (UA, DA).

Accepted manuscript

ACCEPTED MANUSCRIPT

As shown in figure 6e, the AA was added to the PBS containing 5 and 2-fold higher concentration of UA and DA respectively. The figure 6e shows that GO-AMBA-SnO catalyst did not bother the presence of interfering species. The peak resolution of 120, 174, and 294 mV was found between UA – DA, DA – AA and UA – AA respectively. Furthermore, a wide linear range of 4.0×10^{-4}–1.4×10^{-3} M was obtained (figure S4) even with higher sensitivity (885.54 $\mu A m M^{-1} cm^{-2}$) than attained from the individual interfering response of UA and DA. The corresponding linear regression equations are given by;

$I_{pa}\,(\mu A) = 56.297 \times [C_{AA}]\,(mM) + 24.607,\ R^2 = 0.9962$ (in the presence of UA)

$I_{pa}\,(\mu A) = 57.267 \times [C_{AA}]\,(mM) + 24.073,\ R^2 = 0.9987$ (in the presence of DA)

$I_{pa}\,(\mu A) = 62.564 \times [C_{AA}]\,(mM) + 21.327,\ R^2 = 0.9965$ (in the presence of DA and UA)

In PBS solution, at pH 7.4, DA exists in cationic while AA exists in the anionic form. The surface of GO-AMBA-SnO has graphitic–N, which brings the positive charge to its surface. The surface of GO-AMBA-SnO repelled cationic DA, which increased its anodic overpotential. On the contrary, the electrostatic attraction between anionic AA and positively charged GO-AMBA-SnO surface favored the electrooxidation of AA. This effect resulted in a very good resolution of anodic peaks between DA and AA. Different analytical results obtained from electrochemical techniques were compared with a number of already reported biosensors towards AA electrooxidation (table S1). The comparison suggested a far better response of GO-AMBA-SnO nanomaterial towards AA electrooxidation in terms of linear range, LOD and especially sensitivity in the presence of 5 and 2-fold higher concentration of UA and DA interference respectively.

Accepted manuscript

ACCEPTED MANUSCRIPT

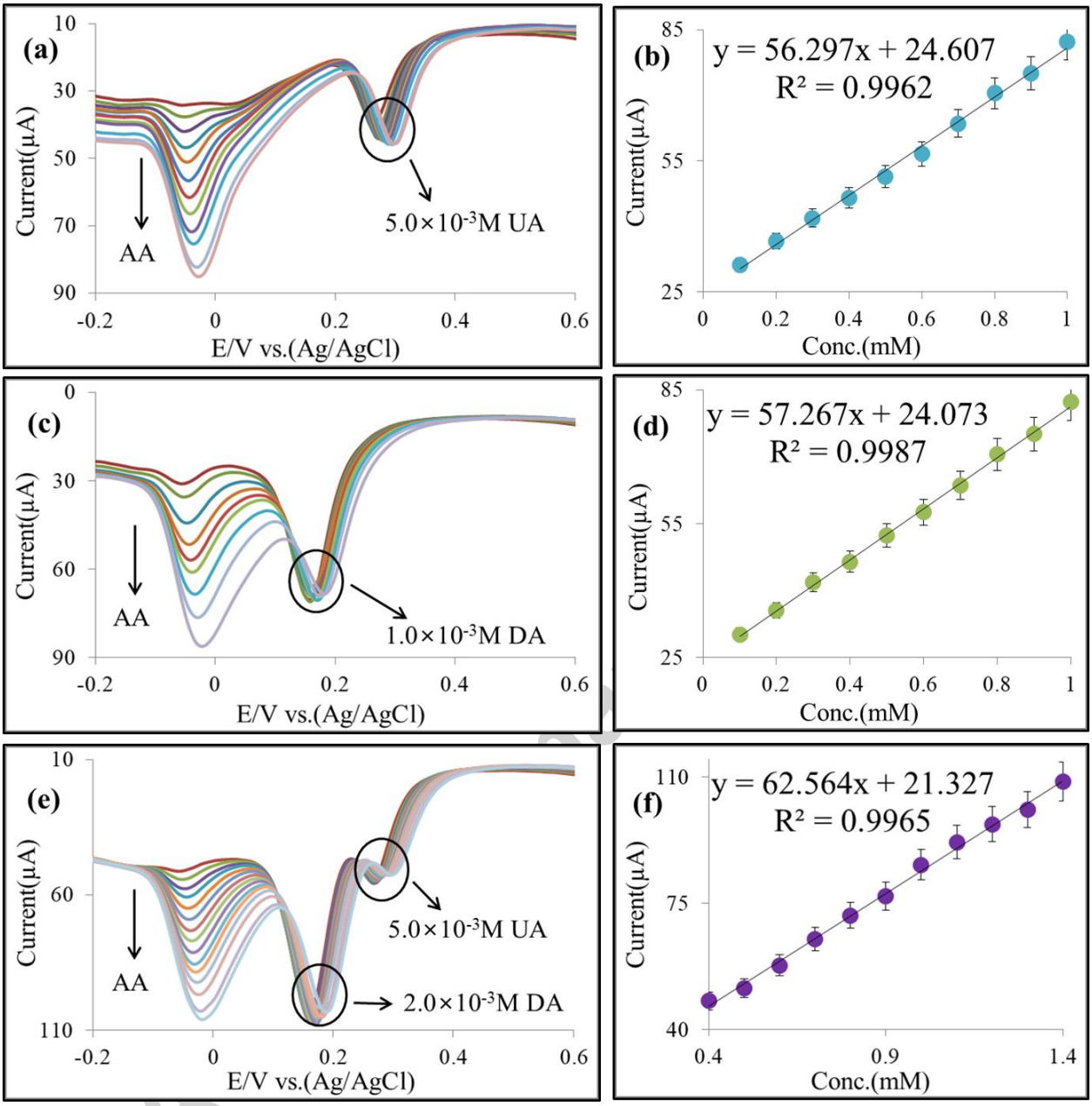

ACCEPTED MANUSCRIPT

Conclusion

Due to the dual valency possession of Sn oxides (SnO_2 and SnO), a new strategy was built for the solo synthesis of SnO in an ethanol-water solvent system on the surface of GO and GO-AMBA. This new strategy will help the scientific community to confidently synthesize SnO and consequently unveil its applications in several fields, as we have explored its role as a biosensor towards AA electrooxidation for the first time. Likewise, there is a great urge for the impeccable synthesis horizon which leads only to the synthesis of SnO_2. Besides, an attempt was made to unveil the factors which lead to the phenomenal pico size of SnO particles. The as-synthesized SnO PPs on GO surface remarkably catalyzed the AA electrooxidation. However, when synthesized on a nitrogen-rich GO surface the electrochemical response was increased up to 29 % due to the synergistic effect of covalent and $\pi - \pi$ stacking interactions of AMBA with GO. The GO-AMBA-SnO catalyst showed a very wide linear range of 5.0×10^{-5}–7.0×10^{-3} M, with LOD of 1.19×10^{-5} M. The sensitivity (885.54 $\mu A m M^{-1} cm^{-2}$) of the catalyst was the most attractive feature, as it was obtained in the presence of 5 and 2-fold higher concentration of UA and DA interfering species respectively.

Accepted manuscript

Acknowledgements

This research was supported by the National Research Foundation of Korea (NRF) funded by the Ministry of Education, Science, and Technology (NRF-2015R1D1A1A09059344).

ACCEPTED MANUSCRIPT

References

Agarwal, A., Shaharyar, A., Kumar, A., Bhat, M.S., Mishra, M., 2015. J. Clin. Orthop. Trauma 6, 101–107.

Ajuria, J., Arnaiz, M., Botas, C., Carriazo, D., Mysyk, R., Rojo, T., Talyzin, A.V., Goikolea, E., 2017. J. Power Sources 363, 422–427.

Chen, H., Ding, L., Sun, W., Jiang, Q., Hu, J., Li, J., 2015. RSC Adv. 5, 56401–56409.

Chen, H., Wang, Q., Shen, Q., Liu, X., Li, W., Nie, Z., Yao, S., 2017. Biosens. Bioelectron. 91, 878–884.

Chen, X.-T., Wang, K.-X., Zhai, Y.-B., Zhang, H.-J., Wu, X.-Y., Wei, X., Chen, J.-S., 2014. Dalton Trans. 43, 3137–3143.

Cobo, S., Heidkamp, J., Jacques, P.-A., Fize, J., Fourmond, V., Guetaz, L., Jousselme, B., Ivanova, V., Dau, H., Palacin, S., Fontecave, M., Artero, V., 2012. Nat. Mater. 11, 802–807.

Derjaguin, B., Landau, L., 1993. Prog. Surf. Sci. 43, 30–59.

Dong, Y., Wang, S., Zhang, T., Zhao, X., Liu, X., Cao, L., Chi, Z., 2013. Brain Res. 1535, 115–123.

Ejaz, A., Ahmed, M.S., Jeon, S., 2016. J. Electrochem. Soc. 163, B163–B168.

Ejaz, A., Jeon, S., 2018. Int. J. Hydrog. Energy 43, 5690–5702.

Ejaz, A., Jeon, S., 2017b. Electrochimica Acta 235, 709–719.

Ejaz, A., Joo, Y., Cho, J.C., Choi, J.M., Kim, J.Y., Lee, S., Jeon, S., 2018a. J. Electroanal. Chem. 813, 31–38.

Ejaz, A., Joo, Y., Jeon, S., 2017. Sens. Actuators B Chem. 240, 297–307.

Ejaz, A., Jeon, S., 2017a. Electrochimica Acta 245, 742–751.

Geffcken, W., Berger, E., Schott, J.G., Jena, G., 1939. , Reichs patent 736411.

Accepted manuscript

ACCEPTED MANUSCRIPT

Geng, D., Yang, S., Zhang, Y., Yang, J., Liu, J., Li, R., Sham, T.-K., Sun, X., Ye, S., Knights, S., 2011. Appl. Surf. Sci. 257, 9193–9198.

Hien, V.X., Lee, J.-H., Kim, J.-J., Heo, Y.-W., 2014. Sens. Actuators B Chem. 194, 134–141.

Ji, D., Du, Y., Meng, H., Zhang, L., Huang, Z., Hu, Y., Li, J., Yu, F., Li, Z., 2018. Sens. Actuators B Chem. 256, 512–519.

Jin, F., Frohman, C., Thannhauser, T.W., Welch, R.M., Glahn, R.P., 2009. Br. J. Nutr. 101, 972–981.

Kiani, F., Razzaghi, Z., Ghadiani, B., Tamizifar, M., Mohmmadi, M.H., Simchi, A., 2017. Ceram. Int. 43, 15010–15017.

Larsen, L.J., Shearer, C.J., Ellis, A.V., Shapter, J.G., 2016. J. Phys. Chem. C 120, 15648–15656.

Lee, W., Kim, M.G., Choi, J., Park, J.-I., Ko, S.J., Oh, S.J., Cheon, J., 2005. J. Am. Chem. Soc. 127, 16090–16097.

Liu, X., Wei, S., Chen, S., Yuan, D., Zhang, W., 2014. Appl. Biochem. Biotechnol. 173, 1717–1726.

Liufu, S.-C., Xiao, H.-N., Li, Y.-P., 2005. J. Colloid Interface Sci. 285, 33–40.

Lu, F., Ji, X., Yang, Y., Deng, W., E. Banks, C., 2013. RSC Adv. 3, 18791–18793.

Luo, H., Liang, L., Cao, H., 2017. Solid-State Electron. 129, 88–92.

Mer, V.K.L., 1952. Ind. Eng. Chem. 44, 1270–1277.

M.matsuo, Japanese patent, 88100032, A2:JP 63100032, May 2, 1988., n.d.

Nagabalasubramanian, P.B., Karabacak, M., Periandy, S., 2011. Spectrochim. Acta. A. Mol. Biomol. Spectrosc. 82, 169–180.

Niederberger, M., Cölfen, H., 2006. Phys. Chem. Chem. Phys. 8, 3271–3287.

Ostwald, W., 1900. Z. Für Phys. Chem. 34U, 495–503.

Paim, A.P.S., Almeida, C.M.N.V., Reis, B.F., Lapa, R.A.S., Zagatto, E.A.G., Costa Lima, J.L.F., 2002. J. Pharm. Biomed. Anal. 28, 1221–1225.

Peng, X., Manna, L., Yang, W., Wickham, J., Scher, E., Kadavanich, A., Alivisatos, A.P., 2000. Nature 404, 59–61.

Pires, F.I., Joanni, E., Savu, R., Zaghete, M.A., Longo, E., Varela, J.A., 2008. Mater. Lett. 62, 239–242.

Accepted manuscript

ACCEPTED MANUSCRIPT

Pisoschi, A.M., Pop, A., Serban, A.I., Fafaneata, C., 2014. Electrochimica Acta 121, 443–460.

Polte, J., 2015. CrystEngComm 17, 6809–6830.

Safaei-Ghomi, J., Shahbazi-Alavi, H., Heidari-Baghbahadorani, E., 2014. RSC Adv. 4, 50668–50677.

Sahbaz, F., Somer, G., 1992. Food Chem. 44, 141–146.

Sakaushi, K., Oaki, Y., Uchiyama, H., Hosono, E., Zhou, H., Imai, H., 2010. Nanoscale 2, 2424–2430.

Senthilnathan, J., Sanjeeva Rao, K., Yoshimura, M., 2014. J. Mater. Chem. A 2, 3332–3337.

Seo, S., Yoon, Y., Lee, J., Park, Y., Lee, H., 2013. ACS Nano 7, 3607–3615.

Shiri, F., Shahraki, S., Shahriyar, A., Majd, M.H., 2017. J. Photochem. Photobiol. B 170, 152–163.

Sinha, B.K., van 't Erve, T.J., Kumar, A., Bortner, C.D., Motten, A.G., Mason, R.P., 2017. Free Radic. Biol. Med. 113, 406–412.

Sliem, M.A., Karas, R.A., Harith, M.A., 2017. J. Photochem. Photobiol. B 173, 661–671.

Song, H., Zhang, L., He, C., Qu, Y., Tian, Y., Lv, Y., 2011. J. Mater. Chem. 21, 5972–5977.

Song, J.-S., Cho, G.-B., Ahn, H.-J., Kim, H.-S., Ahn, J.-H., Cho, K.-K., 2016. J. Nanosci. Nanotechnol. 16, 10735–10739.

Takeuchi, T., 1988. Japanese Patent 88117919 A2:JP 63117919.

Thanh, N.T.K., Maclean, N., Mahiddine, S., 2014. Chem. Rev. 114, 7610–7630.

Therald Moeller [WWW Document], n.d. . Encycl. Br. URL https://www.britannica.com/contributor/Therald-Moeller/2025 (accessed 2.28.18).

Turak, F., Güzel, R., Dinç, E., 2017. J. Food Drug Anal. 25, 285–292.

VerweyOverbeek.pdf, n.d.

Uhlmann, D.R., Zelinski, B.J.J, Wnek, G.E., Brinker, C.J., Clark, D.E., Ulrich, D.R., 1984. Elsevier, New York, 59.

Wang, S.-C., Shaikh, M.O., 2015. Sensors 15, 14286–14297.

Wang, X., Li, K., Yao, L., Wang, C., Van Schepdael, A., 2018. J. Pharm. Biomed. Anal., Review issue 2017 147, 278–287.

Accepted manuscript

ACCEPTED MANUSCRIPT

Wang, Y., Djerdj, I., Smarsly, B., Antonietti, M., 2009. A Chem. Mater. 21, 3202–3209.

Watzky, M.A., Finke, R.G., 1997. Chem. Mater. 9, 3083–3095.

Xu, D., Liu, W., Zhang, C., Cai, X., Chen, W., Fang, Y., Yu, X., 2017.. J. Power Sources 364, 359–366.

Yang, Y., Liu, J., Li, C., Fu, L., Huang, W., Li, Z., 2012. Electrochimica Acta 72, 94–100.

Yoo, B.M., Shin, J.E., Lee, H.D., Park, H.B., 2017. Curr. Opin. Chem. Eng., Nanotechnology / Separation Engineering 16, 39–47.

You, H., Liu, R., Liang, C., Yang, S., Wang, F., Lu, X., Ding, B., 2013. J. Mater. Chem. A 1, 4097–4104.

Zhan, Y., Zhao, R., Meng, F., Lei, Y., Zhong, J., Yang, X., Liu, X., 2011. Mater. Sci. Eng. B 176, 779–784.

Zhang, Huan, Zhang, Honglu, Aldalbahi, A., Zuo, X., Fan, C., Mi, X., 2017. 2D Materials in Biosensors & Bioelectronics 89, 96–106.

Accepted manuscript

ACCEPTED MANUSCRIPT

Fig 1: Schematic illustration of GO-AMBA-SnO nanomaterial synthesis.

Fig 2: HRTEM images of **(a)** GO-AMBA, **(b, c, d)** dispersion of SnO PPs at GO-AMBA surface at different magnification, inset **(c)**: SnO PPs average size measurement, **(e)** EDX spectra of GO-AMBA-SnO, inset: lattice line of SnO PPs, **(f)** EDX elemental mapping of C, N, O and Sn and **(g)** Mechanism of SnO PPs synthesis.

Fig 3: XPS survey spectrum of **(a)** GO-AMBA-SnO nanomaterial, Core-level spectra of **(b)** C1s, **(c)** N1s, **(d)** O1s, and **(e)** Sn3d.

Fig 4: (a) FTIR analysis of GO-AMBA-SnO nanomaterial, inset; close view of FTIR analysis between 500–1000 cm^{-1} frequency, **(b)** XRD pattern of GO-AMBA, and SnO PPs on the GO and GO-AMBA surface, **(c)** Raman spectra of GO-SnO, GO-AMBA and GO-AMBA-SnO nanomaterial.

Fig 5: Cyclic voltammograms recorded in an Ar-saturated 0.1 M PBS (pH, 7.4) at a scan rate of 0.05 Vs^{-1}, curve **(a)**, GO-AMBA-SnO electrode in the absence of AA, curve **(b)** GO-AMBA, curve **(c)**, GO-SnO, and curve **(d)** GO-AMBA-SnO nanomaterial, in the presence of 5.0×10^{-3} M AA.

Fig 6: The DPV response of GO-AMBA-SnO modified electrode for various concentrations of AA in the presence of **(a)** 5.0×10^{-3} M UA, **(c)** 1.0×10^{-3} M DA, **(e)** 5.0×10^{-3} M UA and 2.0×10^{-3} M DA in 0.1 M PBS, and **(b, d and f)** show the respective calibration plots between electrooxidation peak current versus concentration of AA in the presence of interference with 5 % error bar.

Accepted manuscript

ACCEPTED MANUSCRIPT

Highlights

- The role of ethanol solvent in SnO formation was evaluated.
- The application of SnO as a biosensor was studied for the very first time.
- The synergy of dual interactions (covalent and π-π stacking interaction) between AMBA (4-aminomethylebenzylamine) and GO (graphene oxide) was studied.
- The factors responsible for the pico size and monodispersion of SnO particles on GO-AMBA surface was studied exclusively.

Accepted manuscript